Next-Gen Multiband Millimeter-Wave and Terahertz Antennas for Remote Diagnosis of COVID-19 and Dengue via Lung and Glucose Monitoring

Tapan Nahar
Department of Information and Communication Technology, Marwadi University

Sanyog Rawat
Department of Electronics and Communication Engineering, Central University of Rajasthan

https://doi.org/10.5109/7326954

出版情報：Evergreen. 11 (4), pp.3164-3182, 2024-12. Interdisciplinary Graduate School of Engineering Sciences, Kyushu University, Japan
バージョン：

Next-Gen Multiband Millimeter-Wave and Terahertz Antennas for Remote Diagnosis of COVID-19 and Dengue via Lung and Glucose Monitoring

Tapan Nahar[1], Sanyog Rawat[2,*]
[1]Department of Information and Communication Technology, Marwadi University, Rajkot, India
[2]Department of Electronics and Communication Engineering, Central University of Rajasthan, Ajmer, India

*Author to whom correspondence should be addressed:
E-mail: sanyog.rawat@curaj.ac.in

(Received April 30, 2024; Revised August 20, 2024; Accepted October 4, 2024).

Abstract: This paper describes the design of a multiband dual ring antenna, including a 16-element phased array, spatial diversity, and pattern diversity MIMO antennas for future 5G and 6G mm-wave and tera-wave healthcare applications. The proposed antenna array operates at frequencies ranging from 12.991 GHz to 39.966 GHz, 62.114 GHz to 70.452 GHz, 88.04 GHz to 94.7 GHz, and 0.24 to 1 THz and provides moderate gain of 15.2 dB, 16.9 dB, 14.3 dB, 13.4 dB, and 25.5 dB at 28 GHz, 38 GHz, 66 GHz, 92 GHz, and 0.546 THz, respectively, and it encompasses the majority of the 5G mm-wave band, Wi-Gig band, Ku band of satellite communication, W-band, and sub-THz. The proposed antenna array provides strong beam steering capabilities across all operational bands. Spatial diversity and polarization diversity designs provide high isolation bandwidth and impedance bandwidth across all bands, as well as adequate diversity performance for enhanced channel capacity and S/N ratios. The suggested antenna's applications in healthcare are demonstrated. The proposed antenna can detect COVID or illnesses comparable to dengue fever by monitoring the stored water in lung phantoms (a lung infection) and the drop in blood dielectric constant, which implies an increase in blood glucose levels. CST (Computer Simulation Technology) software is used for designing and demonstrating antennas for healthcare applications.

Keywords: COVID’19 (corona virus disease of 2019); fifth generation (5G); multiband antenna; mm-wave antenna; tera-wave antenna; remote healthcare; phased array; beamforming; MIMO antenna

1. Introduction

Millimeter and terahertz frequencies offer enormous potential for remote detection of COVID-infected patients, as well as efficient wireless communication with high speed, low latency, and high reliability used in remote patient monitoring and treatment[1–3]. Terahertz radiation will be used to scan participants' infection of the respiratory pathways with moisture content, which signals edema and is used to distinguish between healthy and infected cells. Terahertz imaging is less dangerous to patients than X-rays; therefore, broad scanning would pose no health problems[2,4]. The identification of dengue disease is proposed in research using a metamaterial-based mm-wave resonator. The disposable top layer can identify dengue by evaluating the dielectric properties of blood samples. With the fall in blood permittivity, the sensor saw a shift in the resonant frequency towards higher frequencies 5G and beyond technology, which uses millimeter wave and terahertz spectrums, is a key necessity for digitally transforming healthcare services[5], so that various issues of currently used communication technologies, such as high latency, limited bandwidth, packet loss, limited data rate, limited capacity, larger antenna size, short battery life, and so on, can be resolved[1,6–8]. By resolving the aforementioned challenges, large-sized health records may be delivered rapidly, and remote monitoring and treatment of patients via video conferencing, remote surgery, autonomous ambulances, and AR-VR systems might be deployed in an effective manner[1,3,6,9]. The currently employed microwave bands cannot meet these requirements due to the high volume of traffic and the high occupancy of other services[10]. Because of the enormous accessible bandwidth in the mm-wave and tera-wave spectrums, efficient communication with a high signal-to-noise ratio can be achievable even in densely populated and loud environments[11,12),3,7,13–16]. Because mm-wave frequencies are impacted and attenuated in the environment, line-of-sight communication is essential to mitigate these difficulties[17].

It is essential to have a high gain and highly directional antenna with a steerable radiation pattern that can sustain a LOS link in all directions[12]. Side lobe levels should be kept low to ensure adequate beam scanning[18,19]. The compact size antenna is necessary for cost reduction[20]. For mm-wave and tera-wave health care communication applications, a multiband antenna array with wide band characteristics, high gain, gain stability throughout bandwidth, compact dimensions, low side lobe levels, and a large scanning range is required [3,21–29]. To be able to deal with several patients with each channel, healthcare applications demand the multiband antenna and related electronics to enable multi-channels. To connect with several sensors at the same time, the channel should have a high bandwidth. As a power harvesting/wireless energy conversion module, a multiband antenna is a viable option for smart healthcare since it can handle both information transmission and integrated smart powering techniques, reducing necessity periodical battery change[26,30]. There have been very few studies in the literature of multiband antenna arrays that cover numerous mm-wave and tera-wave frequencies while maintaining a high steady gain. Some designs have strong bandwidth across many bands yet fluctuate in gain. Some antennas have strong antenna performance, but their multilayer or complicated construction necessitates expensive manufacturing and time-consuming fabrication. Simultaneously achieving broad bandwidth, high and stable gain over wide bandwidth and multiple frequencies, low side lobe levels, and wide beam steering range is extremely challenging with a compact, simple, planer, low profile, and cost effective structure which is required to enable efficient wireless communication without affecting from atmospheric, other propagation losses, and power limitations issues[21,31,32]. Fabrication imperfections, alignment problems, and inexpensive and time-consuming fabrications are also critical aspects to consider at THz and mm-wave frequencies[33].

To rectify the above research gap, low-cost, low-profile, planer, compact, ultra-wideband, narrow beam, steerable, and multiband antenna, its beam steering array, spatial diversity and pattern diversity antennas are proposed which cover the majority of the 5G mm-wave band, Wi-Gig band, Ku band of satellite communication, W-band, and sub-THz spectrum and proposed for future 5G and beyond wireless applications. The proposed antennas could be a good candidate for a variety of health care applications, including remote monitoring of COVID patients, remote health care services, wireless monitoring of blood sugar detection, driverless ambulance, efficient indoor communication in crowded environments, mm-wave and tera-wave imaging and spectroscopy, AR-VR based healthcare services, remote drug delivery, automatic facture detection, remote robotic surgery, and many more. This work proposes a 16-element compact planner array with an extremely wide bandwidth of 96.33 percent from 12.991 GHz to 39.966 GHz, 12.63 percent from 62.114 GHz to 70.452 GHz, 7.23 percent from 88.04 to 94.7, and 140.74 percent from 0.24 to 1 THz. To the best of the author's knowledge, this form of multiband antenna will be the first to be suggested in literature and will be capable of operating on the higher mm-wave bands suggested for 5G as well as the sub-THz band with beam steerable characteristics. All the antenna structures are simulated on computer simulation technology microwave studio (CST Microwave studio)[34]. With planner geometry, lightweight, low profile, less complicated and compact size, the discussed antenna delivers good gain, narrow beam width, low side lobe levels, and broad beam steering range.

This paper is divided into eight sections. Section 1 explains the mm-wave and tera-wave antenna requirements in health-care systems. Section 2 depicts the development of the suggested antenna design. Section 3 shows the simulation results of single antenna elements. Section 4 illustrates the realization of the 16-element array and beam steering performance. Section 5 contains results of beam steering array. Section 6 contains performance comparisons with previously published mm-wave antennas. Section 7 presents MIMO configurations and results. Healthcare applications and specifically blood sugar fluctuation and lung infection detection by the proposed multiband antenna is showcased in section 8. Section 9 concludes the paper.

2. Evolution of proposed antenna design

Firstly, a 28 GHz rectangular patch antenna with dimensions of 4.2x3.47 mm^2 is designed on a Roggers RT 5880 substrate with a dielectric constant of 2.2, a loss tangent of 0.0009, and a thickness of 0.254 mm. A 0.78 mm wide 50-Ohm microstrip line feeds the patch. At 27.532 GHz, the rectangular patch antenna gives 2.07 percent bandwidth. A rectangular slot of 2.2x1.47 mm^2 is constructed at the middle of the rectangular patch to increase bandwidth, and a partial ground plane length of 2.46 mm is employed. Geometry is simulated on CST Microwave Studio[34]. According to[35], loss tangent of Roggers RT 5880 is increased at THz but it is varied from 0.002 to 0.016 at THz frequencies frequencies from 0.2 to 1 THz and Dielectric constant varies between 2.27 to 2.3. It may be used for THz frequencies. Rectangular slots introduce capacitive reactance into the input impedance, reducing the feed line's inductive impedance. Similarly, a partial ground plane generates capacitive reactance, which reduces the radiator's inductive reactance. The bandwidth is increased by carefully adjusting the ground plane length and slot dimension[14]. ANT1 is the term given to this 28 GHz rectangular slotted rectangular microstrip antenna, which is seen in Fig. 1 (a). Similarly, as shown in Figure 1 (b), a rectangular slotted rectangular microstrip antenna with a partial ground plane is designed for a 66 GHz resonant frequency and is referred to as ANT2. The dimensions of the rectangular patch, rectangular slot and ground plane length are 1.69×1.3 $mm^{2,}$ 1.19×0.8 mm^2 and

1.59 mm. ANT3 is created by placing a tiny 66 GHz ANT2 in the middle of a 28 GHz ANT1. The top layer and bottom layer geometries are depicted in Fig. 1 (c) and (d), respectively. The large ground plane length is the same as ANT1's 2.46 mm. A 2.2x2 mm^2 small ground plane is designed. A tiny air gap of 0.191 mm is maintained between the big and small ground planes.

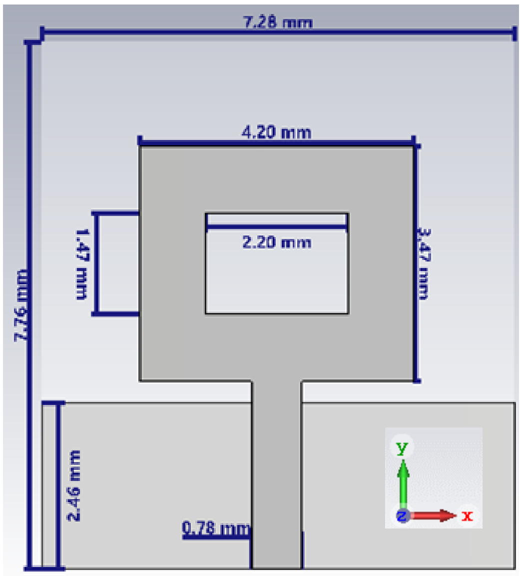

(a)

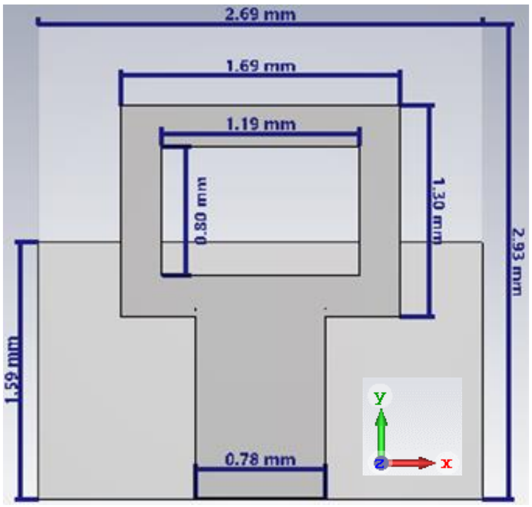

(b)

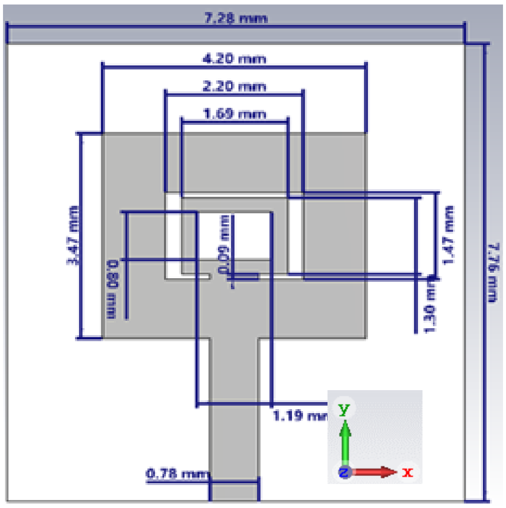

(c)

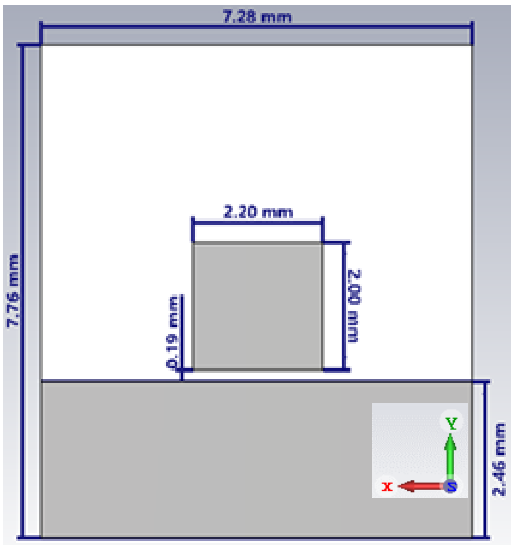

(d)

Fig. 1: Geometry of (a) ANT1 (rectangular slotted microstrip antenna at 28 GHz)[14] (b) ANT2 (rectangular slotted microstrip antenna at 66 GHz) (c) Top View of ANT3 (Multiband dual rectangular ring antenna) (d) Bottom view of ANT3

3. Simulation results of designed geometries

The simulated reflection coefficient (S 11) versus frequency plot is used to evaluate impedance matching ability at various frequencies. S 11 is the reflected power to incident power ratio. S 11 should be less than -10 dB at a working bandwidth. Figure 2 (a) and 2 (b) show S 11 versus frequency plots of ANT1, ANT2, and ANT3 for frequency ranges of 1-100 GHz and 0.1-1 THz, respectively.

It may be noted that ANT1 resonates between 12.797 and 35.208 GHz and delivers 140.386 percent bandwidth at 15.864 GHz. At higher frequencies between 85 and 93 GHz, a very tiny band with substantial return loss is achieved, which is avoided due to larger than 12 dB of return losses. ANT1 additionally has an operating frequency band of 0.21-1 THz and a bandwidth of 130.57

percent with a central frequency of 0.605 THz.

ANT2 is tuned from 60.63 GHz to 74.067 GHz and 0.2688 to 1 THz, providing 20.09 percent bandwidth at 66.88 GHz and 124.52 percent bandwidth at 0.6344 THz. ANT 3 is an integrated two-ring microstrip antenna that resonates over all four ANT1 and ANT2 operational frequencies. From 12.991 GHz to 39.966 GHz, 62.114 GHz to 70.452 GHz, 88.04 GHz to 94.7 GHz, and 0.24 to 1 THz, ANT3 gives S 11 less than -10 dB. At 28 GHz, 66 GHz, 92 GHz, and 0.54 THz, the impedance bandwidth of ANT3 is 96.33 percent, 12.63 percent, 7.23 percent, and 140.74 percent, respectively. As a result, the proposed antenna ANT3 covers the 5G communications bands of 28 GHz, 38 GHz, and 66 GHz, as well as the 94 GHz and lower THz range (0.24-1 THz) for 5G beyond and future wireless communication systems.

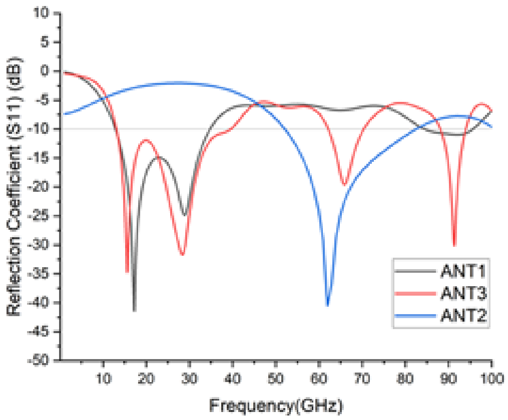

(a)

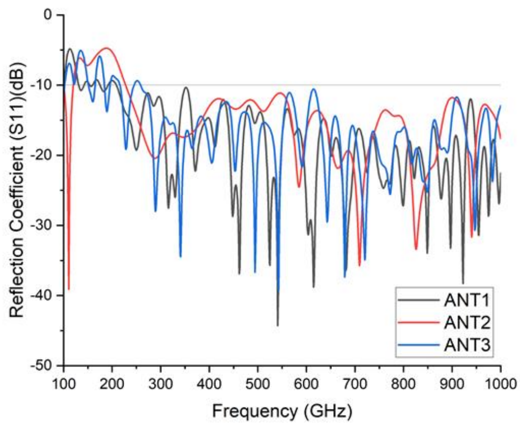

(b)

Fig. 2: Consolidated Reflection Coefficient (S 11) versus frequency plot (a) for 0.1-100 GHz range (b) for 0.1-1 THz range

Figure 3(a) and (b) show gain versus frequency plots for frequency ranges of 10-100 GHz and 0.1-1 THz, respectively. At operational frequencies, at 28 GHz, 38 GHz, 66 GHz, and 92 GHz, ANT3 delivers gain of 2.8 dB, 1.8 dB, 2 dB, and 4.7 dB, respectively. The gain of ANT3 ranges between frequencies of 0.24-1 THz, ranging from 10.05 to 15.81 dB. It may be observed that the variation in antenna gain is less than 3 dB at operating bands in mm-wave band. Out-of-band rejection is beneficial for the antenna's performance. Out-of-band rejection indicates that the antenna's gain is lowered at frequencies where it is not resonating or has a reflection coefficient larger than -10 dB. Between 45 and 60 GHz, the antenna has a negative gain. Because the gain of ANT3 ranges between 2 and 4.9 dB for working bands of frequencies 10-100 GHz, which is quite small, a 16-element array is realized to improve gain.

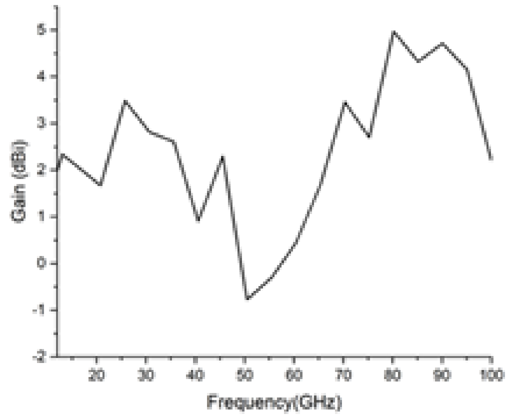

(a)

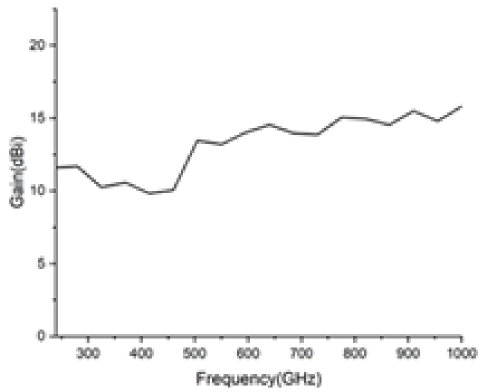

(b)

Fig. 3: Gain versus frequency plot of ANT3 (a) for 10-100 GHz (b) for 0.24-1 THz

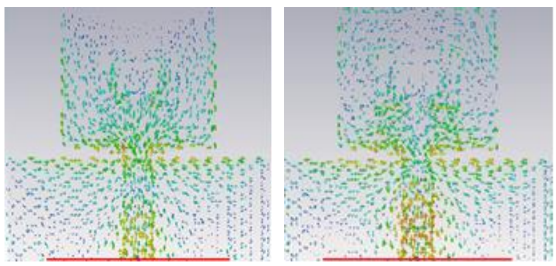

(a) (b)

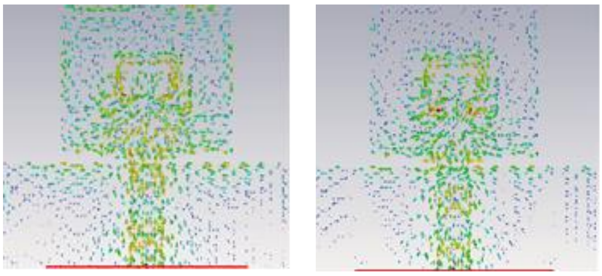

(c) (d)

Fig. 4: Surface current distribution of proposed ANT3 (a) at 28 GHz (b) at 38 GHz (c) at 66 GHz (d) at 92 GHz (e) at 0.54 THz

Figure 4 (a) through (e) illustrate the surface current distribution of the proposed ANT3 at various frequencies: 28 GHz, 38 GHz, 66 GHz, 92 GHz, and 0.54 THz. At 28 GHz, the maximum surface current is 258.07 A/m and is prominently observed along the outer rectangular ring and the large partial ground edges adjacent to the patch. At 38 GHz, the peak current increases to 291.36 A/m and is similarly concentrated around the outer rectangular ring and the large partial ground edges. For 66 GHz, where the maximum current reaches 293.63 A/m, the distribution shifts to the inner rectangular ring and a smaller partial ground area located beneath this ring. At 92 GHz, the surface current peaks at 575.81 A/m and is primarily concentrated within the inner portion of the inner rectangular ring. This pattern continues at 0.54 THz, with the peak current of 351 A/m also being concentrated in the inner portion of the inner rectangular ring. These observations reveal how the surface current distribution evolves with frequency, showing distinct regions of maximum current concentration and their shifts across different operating frequencies. The maximum surface current density of an antenna is crucial for its performance and functionality. High density indicates efficient operation, stronger signal transmission, and increased radiation efficiency. It affects radiation pattern and gain, directivity, and gain. Understanding current density distribution helps engineers optimize antenna design by adjusting dimensions, materials, and configurations to enhance performance characteristics like gain and impedance matching. It also assesses the antenna's power handling capability and is essential for designing effective impedance matching networks. Accurate knowledge of current density is essential for optimizing antenna performance and achieving desired operational characteristics across different frequencies.

4. Simulation of a 16-element multiband beamforming array

A 16 element array is simulated on CST Microwave Studio[34)] to improve the gain of a multiband array. Figure 5 (a) and (b) depict the top and bottom views of a simulated 16 array.

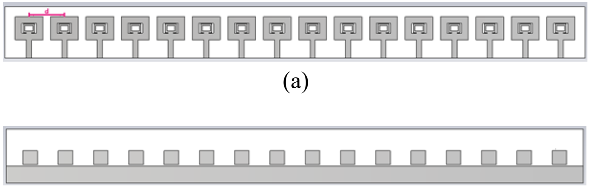

(a)

(b)

Fig. 5: (a) Top view of 16 element array of ANT3
(b) Bottom view of 16 element array of ANT3

The selection of inter-element spacing (d) in a wideband array is extremely challenging. The wavelength influences the inter-element spacing. The operational wavelength of the proposed wideband array changes from 7.55 mm to 21.73 mm in the first band, 4.268 mm to 4.83 mm in the second band, and 3.16 to 3.40 mm in the third band. In this regard, spacing is very carefully chosen because when spacing satisfies performance in one band, performance in the other band suffers. The spacing between elements should be higher than half a wavelength to one wavelength. The most commonly used center frequencies are 28 GHz, 38 GHz, 66 GHz, and 92 GHz. Our goal is to choose inter-element spacing in such a way that performance in all four bands may be optimized. Table 1 shows the effect of varying spacing on performance characteristics at all four frequencies. The wavelength ranges from 0.4 λ_1 to λ_1. λ_1 is a wavelength at 28 GHz. At 28 GHz, a maximum gain of 18.4 dB is achieved with a spacing of 0.9 λ_1, but side lobe levels are high and gain is low. At 0.65 λ_1 or 0.88λ_2 spacing, the array gain is 18.8 dB at 38 GHz, however, at 66 GHz, the gain is minimal and side lobe levels are high. λ_2 is the wavelength at 38 GHz. Gain of 14.3 is attained at 66 GHz with spacing of 0.4λ_1 or 0.94λ_3, while gain is modest in other bands with low side lobe levels. At 66 GHz, λ_3 is the wavelength. At 92 GHz, a maximum gain of 15.9 dB is attained with a spacing of 0.85$\lambda_1$or 2.8λ_4, however the main lobe angle is 135 degrees and side lobe levels are strong. Our goal is to achieve maxima at 0 or 180 degrees in all 4 bands while maintaining high gain and low side lobe levels. The average wavelength of λ_1, λ_2, λ_3, and λ_4 is 6.6 mm. Spacing of 0.4λ_1 may be expressed as 0.65 λ_{avg} or 0.65×6.6, indicating that the best spacing is between 0.5λ to λ.

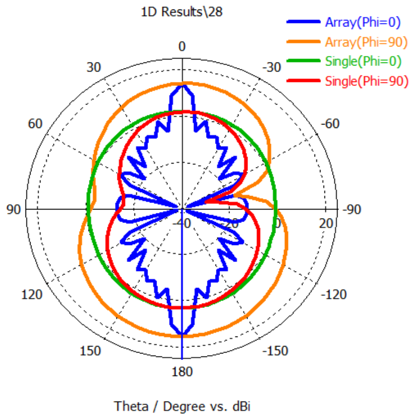

(a)

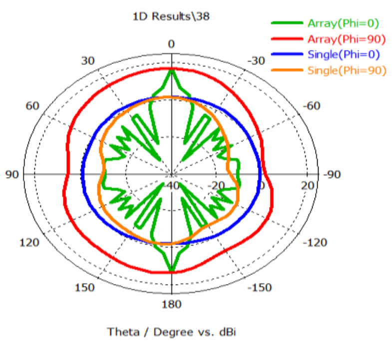

(b)

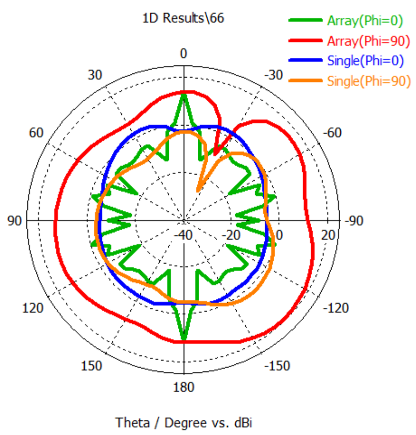

(c)

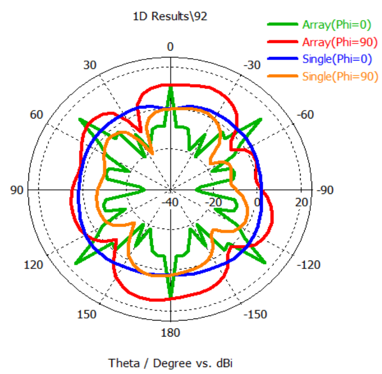

(d)

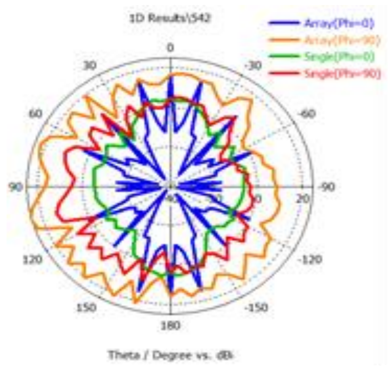

(e)

Fig. 6: Consolidated radiation pattern of single and 16 element array of ANT3 (a) at 28 GHz (b) at 38 GHz (c) at 66 GHz (d) at 92 GHz (e) at 0.54 THz

Figure 6(a), (b), (c), (d), and (e) show the consolidated radiation patterns of the proposed ANT3 and its 1*16 array at Phi=0 and 90 degrees for frequencies 28 GHz, 38 GHz, 66 GHz, 92 GHz, and 0.54 THz, respectively. The radiation pattern in Fig. 6(a) is quasi-bidirectional. At 28 GHz, two maxima were achieved with gain differences of 1 dB at angles of 0 and 180 degrees. A maximum gain of 15.2 dB is obtained at Phi=0 and Theta=0 with a relatively narrow beamwidth of 6 degrees at 28 GHz. When these two lobes are considered main lobes, the other side lobe level is -15.6 dB. At Phi=0, a beamwidth of 6 degrees is obtained. The beamwidth at Phi=90 is quite big. When the radiation pattern of a 1*16 array is compared to the radiation pattern of a single element, the gain and directivity rise while the beamwidth decreases. Figure 6(b) shows that at 38 GHz, a quasi-bidirectional radiation pattern of 1*16 array with two maxima and a gain difference of 3.5 dB is obtained at Phi=0. Other side lobe values are less than -21.6 dB when two maxima at angles of 0 and 180 degrees are included. The maximum gain of 16.9 dB is obtained at Phi=0 and Theta=0 with an extremely small beam width of 2.8 degree. At Phi=90, a wide beam width of 61 degrees is achieved. In this manner, a directional pattern is obtained in one plane while covering a wide range of angles in the other. The pattern is similar to a bidirectional fan beam. Figure 6(c) depicts the radiation performance at 66 GHz. At Phi=0, a quasi-bidirectional radiation pattern of 1*16 array with two peaks of gain difference 3 dB is obtained. At Phi=0 and Theta=0, a gain of 14.3 dB with a beam width of 2.3 deg. is obtained. The values in the other side lobes are less than -15.38 dB. A highly directive narrow beam with a large range of coverage in the opposite plane is achieved. As shown in Figure 6(d), the radiation pattern of 1*16 array at 92 GHz has numerous maxima in 6 directions, a gain of 13.4 dB, and a beam width of 1.3 degree at Phi=0 and Theta=0. There is a 2 dB gain difference between the radiation pattern maxima in the upper and lower halves of the plane. If all maxima's are considered as main lobes, side lobe values are around -9 dB. The radiation pattern at Phi=0 and 90 degrees at 0.54 THz is depicted in Fig. 6 (e). Figure 6(e) shows that the pattern of 1*16 array contains several lobes, a beamwidth of 1 degree, and a maximum gain of 25.5 dB. Several beams are important for receiving radiation from multiple directions, but they can adversely affect the signal-to-noise ratio. Side lobes are quite strong and should be reduced. As may be seen in Fig. 7 Beamwidth is approximately 11.4 degrees at Phi=90 degrees, while maximum gain is attained at 105 degrees. Figure 7 shows a gain versus frequency plot of a 16-element array at 10 to 100 GHz. It can be seen that the gain varies by less than 5 dB over the whole operational frequency spectrum.

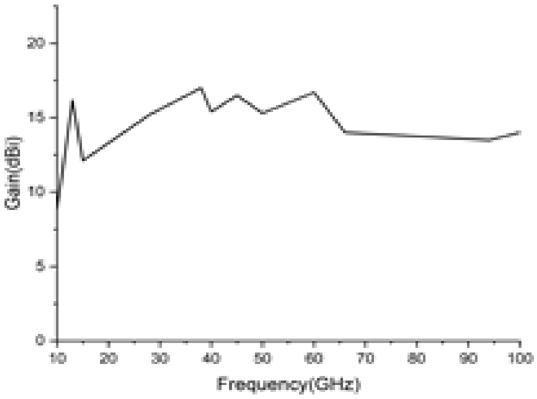

Fig. 7: Gain versus frequency plot of 16 element array

Table 1. Effects of inter-element spacing on performance of 16 element multiband array

Inter-element Spacing (d) (mm)	At 28 GHz				At 38 GHz				At 66 GHz				At 92 GHz			
	Gain (dB)	Main Lobe Angle (deg.)	Beam-Width (deg.)	SLL (dB)	Gain (dB)	Main Lobe Angle (deg.)	Beam-Width (deg.)	SLL (dB)	Gain (dB)	Main Lobe Angle (deg.)	Beam-Width (deg.)	SLL (dB)	Gain (dB)	Main Lobe Angle (deg.)	Beam-Width (deg.)	SLL (dB)
10.7×.4	15.2	180	6	-16.2	16.9	0	2.8	-21.5	14.3	0	2.3	-15.5	13.4	180	1.3	-9
10.7×.5	16.1	180	3.5	-21.4	17.9	0	1.2	-22.0	9.7	0	2.1	-1.7	14.7	180	1.7	-1.1
10.7×.6	16.9	180	2.1	-24.4	18.6	0	1.6	-23.1	13.1	45	2.3	-2.5	14.8	30	1.7	-1.7
10.7×.65	17.3	180	1.5	-26.6	18.8	0	2	-21.4	13.3	40	1.7	-2.4	13.7	115	2	-0.7
10.7×.7	17.6	180	0.9	-24.8	18.7	0	2.2	-15.8	10.8	0	1.7	-11.8	15.5	25	1.2	-0.9
10.7×.75	17.8	180	1.1	-25.7	13.7	0	2.3	-2.5	13.9	35	1.4	-3.1	13.6	180	1.5	-1.1
10.7×.8	18.1	180	1.5	-24.1	12.8	0	2.2	-2.8	10.7	0	1.7	-10.7	13.8	180	1.3	-1.1
10.7×.85	18.3	180	1.8	-21.2	12.6	0	2.1	-1.7	14.3	30	1.7	-4.4	15.9	135	1.2	-1.6
10.7×.9	18.4	180	2	-18.2	12.6	0	1.8	-1.4	9	0	.8	-1.7	12.7	180	1.2	-1.1
10.7×.95	18.4	180	2.2	-16.9	12.6	0	1.5	-1.5	9	0	1.1	-3	14.4	110	2	-1.6
10.71×1	15.8	180	2.3	-3.7	12.7	0	1.2	-3.5	13.6	25	1.1	-4.5	13.1	180	1.3	-1.1
10.7×.95	18.4	180	2.2	-16.9	12.6	0	1.5	-1.5	9	0	1.1	-3	14.4	110	2	-1.6
10.71×1	15.8	180	2.3	-3.7	12.7	0	1.2	-3.5	13.6	25	1.1	-4.5	13.1	180	1.3	-1.1

5. Beamsteering performance of proposed array at multiple bands

A steerable narrow beam radiation pattern is necessary to preserve line of sight connection. Beamforming is a technology, which controls data transmission and reception in certain angles. It has several uses in medical. It improves the spatial accuracy and quality of images in clinical imaging methods, allowing for improved 3D and 4D imaging. This also enhances the efficiency of wearable health surveillance equipment and Body Area Networks (BANs) by reducing noise and increasing communication reliability. Beamforming also improves the strength of signals for remote patient monitoring by increasing data transfer and lowering interference. It improves communication in telemedicine by enhancing visual and audio conversations between healthcare practitioners and patients. It enhances communication in implanted devices, hence increasing data reliability and precision. It also improves location tracking in emergency medical services, allowing for more effective data exchange and coordination. Beamforming also improves communication in medical robots, enabling more accurate and synchronized motions. Multibeam and bidirectional radiation patterns improve scanning precision and reach, enabling more accurate diagnosis and therapy. In radiation treatments, it allow for focused cancer treatment while sparing tissues that are healthy. Such patterns also enhance energy supply and reception of signals in healthcare devices, resulting in more efficient and consistent operation. Overall, they help to improve patient outcomes and provide more effective healthcare solutions.

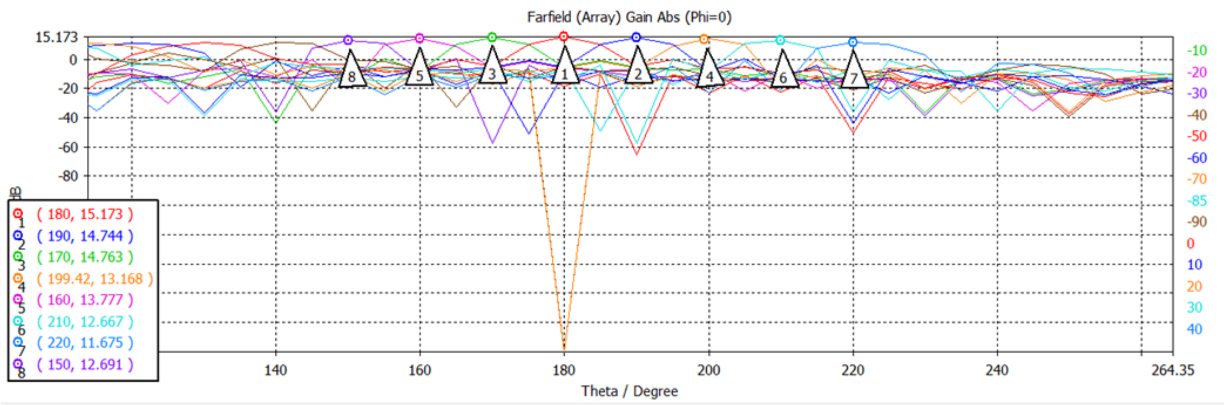

(a)

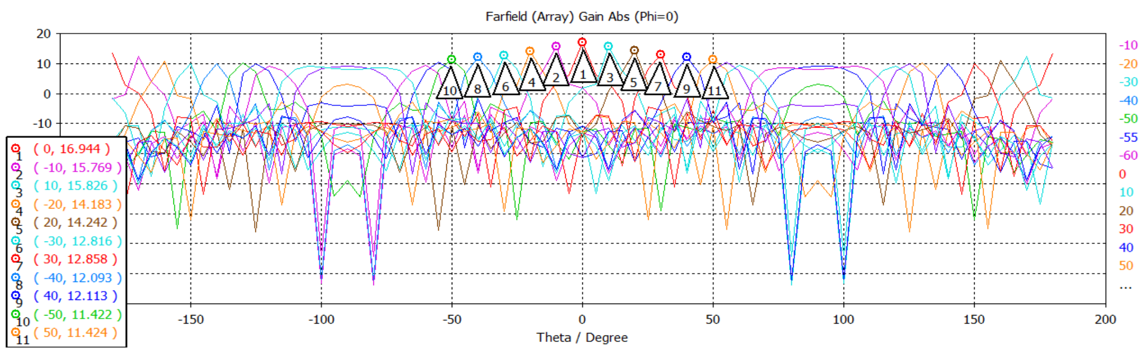

(b)

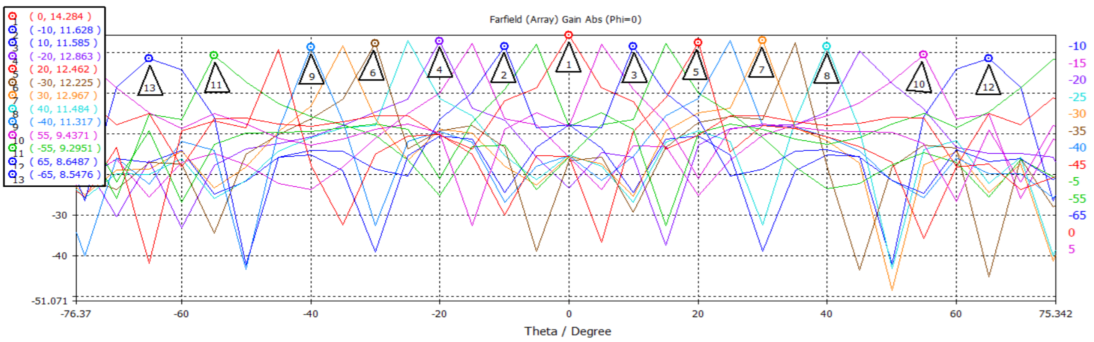

(c)

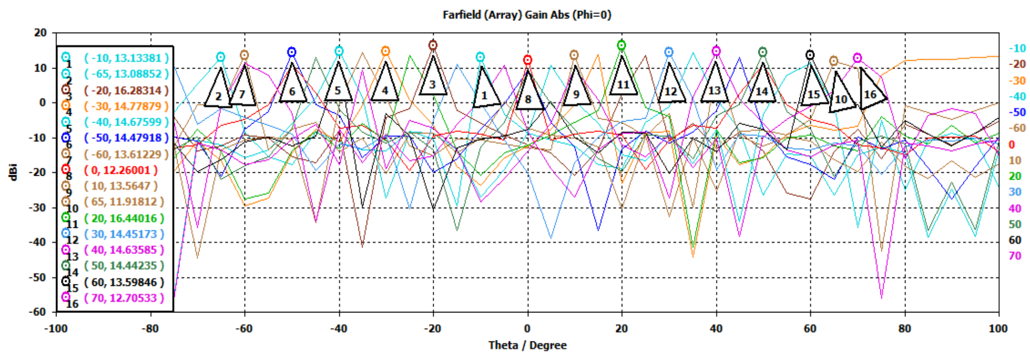

(d)

Fig. 8: Gain at ϕ=0 variation of proposed antenna array at different scanning angles (a) at 28 GHz (b) at 38 GHz (c) at 66 GHz (d) at 92 GHz

To accomplish a wide range of beam scanning, the beamwidth should be narrow and the side lobe levels should be less than -10 dB. At all scanning angles, scanning loss should be minimal. Figure 8 (a), (b), (c), and

(d) illustrate the beamsteering performances of the proposed multiband antenna array at 28 GHz, 38 GHz, 66 GHz, and 92 GHz, respectively. A plot of the relationship between gain (Phi=0) and scanning angle is shown. According to Figure 8(a), side lobe levels at 28 GHz are less than -10 dB for scanning angles ranging from -90 to +85 degrees. At a scanning angle of 180 degree, a maximum gain of 15.2 dB is obtained. It is considered as main lobe and scanning angles are considered from this center. Scanning losses of less than or equal to 3 dB are found at scanning angles of -30 to +30 degrees and ±85 to ±90 degrees. At 28 GHz, scanning loss is less than 4 dB from -90 to +90 degrees. For scanning angles ranging from -40 to +40 degrees, the beamwidth is less than 10 degrees. Maximum gain of 16.944 dB is reached at 38 GHz at a scanning angle of 0 degree, as shown in Fig. 8(b). At beam scanning angles ranging from -20 to +20 degrees, scanning loss is less than or equal to 3 dB. At 38 GHz, scanning loss of less than 5 dB was obtained throughout a scanning range of -40 to +40 degrees. At a scanning range of -40 to +40 degrees, side lobe levels are less than -10 dB and beamwidth is less than 10 degrees. Figure 8(c) depicts beamsteering performance at 66 GHz. At 66 GHz, a maximum gain of 14.3 dB is obtained at a scanning angle of 0 degree. At scanning angles ranging from -40 to +40 degrees, less than 3 dB of scanning loss and less than 3 degrees of beamwidth are attained. Multiple maxima obtained at particular scanning angles are significant variances in beamsteering performance at 66 GHz compared to other bands. If numerous maxima are not taken into account, side lobe levels are high. For example, when the beam is scanned at +5, a gain of 12.127 dB is obtained, with further maxima at 175 and -100 degrees. Multibeam performance is beneficial for 5G, although it raises the signal-to-interference ratio. Figure 8(d) depicts beamsteering performance at 92 GHz. It is possible to obtain a multibeam radiation pattern. At a scan angle of 20 degrees, the maximum gain is 16.44 dB. The beamwidth is less than five degrees. Scanning loss of less than or equal to 3 dB is obtained at 10 degrees to 60 degrees and -20 degrees to -60 degrees. At all scan angles, the beamwidth is very small (5 degrees). Scan angles ranging from -65 to 70 degrees result in less than 5 dB of scanning loss.

6. Comparisons with other reported millimeter wave and THz antennas

Comparative Table 2 compares the performance of the proposed multiband antenna to that of previously published 28 GHz arrays. In comparison to published antennas at 28 GHz, the suggested antenna features a compact size, wide bandwidth, high gain, small beamwidth, and low side lobe levels. Beamsteering range needs to be increased when compared to other reported antennas[36)] and[37)]. Table 3 compares the performance of the proposed multiband antenna to that of previously reported 38 GHz antennas. It can be seen that the proposed multiband antenna performance is better than existing reported 38 GHz antennas in terms of gain, bandwidth, scan range, and side lobe levels. Performance of proposed multiband antenna is also compared with reported antennas operating between 60 to 70 GHz bands which are shown in Table 4. The suggested multiband antenna's performance is also compared to published antennas operating in the 60 to 70 GHz band, as shown in Table 4. The proposed antenna has a greater bandwidth than[38),39)] and[40)], however it has a lower gain. The suggested multiband antenna has a higher gain than the two structures reported in[39)], but its bandwidth is limited in comparison. The proposed antenna's beamwidth, side lobe levels, and dimensions are all less than those of previous antennas. Table 5 shows performance comparisons with reported antennas at 92 GHz. In comparison to previously published research[41–43)], the suggested antenna provides strong gain, small beam width, and good beam scanning range. Table 6 compares performance with reported sub-THz antennas. In compared to prior studies[44–46)] the proposed antenna has a high gain, a narrow beam width, and a wide bandwidth. Because of the multiband operation, the size of the antenna is larger than that of other antennas, but the merits of the proposed antenna include a single layer, a planar construction, and a low profile. The suggested antenna's overall performance in all the bands (28 GHz, 38 GHz, 66 GHz, 92 GHz, and 0.54 THz) is suitable for 5G and beyond applications.

7. Multiband MIMO Design

Wide band multiple input multiple output antennas can help overcome two significant challenges in 5G communication: restricted channel capacity and Signal to Noise Ratio. The Shanon Chennal Capacity Theorem states that increasing bandwidth and signal to noise ratio will increase capacity.

Table 2. Performance comparisons with reported 28 GHz antennas

Works	**Size (mm^3)**	**No. of elements**	**Single layer (S)/ Multi-layer (M)**	**No. of bands**	**Band1 (28GHz)**							
					FL1 (GHz)	**FH1 (GHz)**	**FR (GHz)**	**BW %**	**Gain (dB)**	**Beam - width (deg.)**	**Scan Range (deg)**	**SLL (dB)**
Proposed	8.518×72.77× 0.254=157.44	1×16	S	Four	12.991	39.966	28	96.33	15.2	6	-30 to +30 ±85 to ±90	- 15.6
36)	51.3×4×1.5 =318.6	1×8	S	One	27.5	30	28	8.92	15.6	10	±60°	-12
37)	140 × 140 × 3.754=73578.4	4	M	One	26.5	31.5	29	18	11.2	15	±90	
47)	66 × 15 × 0.3=3069	1×8	S	One	24	29	26	21.15	12	13.3	NA	-15
48)	45.48× 21.79 × 0.5952=589.84	1×8	S	One	24.15	28.5	26	16.99	11.9	8	NA	-10
49)	26.31× 26.31× .25=173.05	3×3	S	One	27.3	29	28	7	14.9	34	±25	-9.5

Table 3. Performance comparisons with reported 38 GHz antennas

Works	**Size (mm^3)**	**No. of elements**	**Single layer (S)/ Multi-layer(M)**	**No. of bands**	**Band1 (38GHz)**							
					FL1 (GHz)	**FH1 (GHz)**	**FR (GHz)**	**BW %**	**Gain (dB)**	**Beam-Width (deg.)**	**Scan Range (deg.)**	**SLL (dB)**
Proposed	8.518×72.77× 0.254=157.44	1×16	S	Four	12.991	39.966	28	96.33	16.9	2.8	±20	- 21.64
22)	13×20×.254=66	8	S	Two	36	38.5	38	6.57	13.46	-	-	-12
25)	21×26×0.8=436.8	3×3	S	Three	35.5	40	38	11.84	9.58	-	-	-
50)	87.4×24.1×1.77 =3728.22	13	S	Two	35.5	39.15	38	9.78	15.6	-	-	-
51)	43.611×43.611×0.4 =760.7	2×4	S	Two	37	37.6	37	1.62	13.7	-	-	-

Table 4. Performance comparisons with reported 66 GHz antennas

Works	**Size (mm^3)**	**No. of elements**	**Single layer (S)/ Multi-layer (M)**	**No. of bands**	**Band2 (66 GHz)**							
					FL2 (GHz)	**FH2 (GHz)**	**FR (GHz)**	**BW %**	**Gain (dB)**	**Beam Width (deg.)**	**Scan Range (deg.)**	**SLL (dB)**
Proposed	8.518×72.77× 0.254=157.44	1×16	S	Four	62.11	70.452	66	12.63	14.3	1.3	-40 to +40	-15.38
38)	41×13×.3556 =189.53	4×16	M	One	57	65	60	12.30	18.7	7		
39)	13410.434	4×16	M	One	60	66	60	9.8	20.8	7	±50	
39)	13240.434	4	M	One	56.5	66	60	15.4	12		NA	
40)	14×14×0.925 =181.3	16	M	One	57.2	64.4	62	11.61	18.1			

Table 5. Performance comparisons with reported 92 GHz antennas

Works	**Size (mm^3)**	**No. of elements**	**Single layer (S)/Multi-layer (M)**	**No. of bands**	**Band3 (92 GHz)**							
					FL3 (GHz)	**FH3 (GHz)**	**FR (GHz)**	**BW %**	**Gain (dB)**	**Beam Width (deg.)**	**Scan Range (deg.)**	**SLL (dB)**
Proposed	8.518×72.77× 0.254=157.4	1×16	S	Four	88.04	94.7	92	7.23	13.4	2.3	10 to 60 -20 to -60	-9
41)	-	-	S	One	85	110	-	6.5	-	10±3	13 to 55	10
42)	16×11×.236= 41.536	1×4	M	One	91.5	96.5	94	5.31	13	20	-	<-10
43)	-	1×4	M	One	80	110	94	31.91	4.43	-	-	-5

Table 6. Performance comparisons with reported THz antennas

Works	**Size (mm3)**	**No. of elements**	**Single layer (S)/Multi-layer (M)**	**No. of bands**	**Band4 (0.54 THz)**							
					FL3 (THz)	**FH3 (THz)**	**FR (THz)**	**BW %**	**Gain (dB)**	**Beam Width (deg.)**	**Scan Range (deg.)**	**SLL (dB)**
Proposed	8.518×72.77×0.254=157.44	1×16	S	Four	0.24	1	0.54	140.7	25.5	1	-	-2.3
44)	2.6*2.6*1.24=8.38	1	M	One	0.282	.304	0.3	7.33	17.7	-	-	<-15
45)	2.8*3.2*2.7=24.192	1	M	One	0.23	.33	0.3	33.33	18	24	-	-
46)	-	5*4	S	One	0.294	0.376	0.3	27.33	13.6	55	-	-10.2

A MIMO antenna has many antennas to increase channel capacity, signal to noise ratio, and provide an additional communication path. Multiband antenna design is a difficult task in MIMO antennas. Spatial diversity and pattern diversity MIMO setup is meant to address this. Isolation must be less than 10 dB over a broad bandwidth and all diversity parameters must fall into an acceptable range for MIMO operation to be effective.

Front view and back view of Spatial diversity MIMO (SD-MIMO) and polarization diversity (PD-MIMO) antenna are presented in Fig. 9(a), Fig. 9(b), Fig. 9(c), and Fig. 9(d). In the SD-MIMO (Substrate-Driven Multiple Input Multiple Output) antenna design, two rectangular ring antennas are positioned with a separation distance of 5.38 mm. A rectangular decoupling element, which has a width of 0.5 mm, is placed between the two adjacent antennas.

This decoupling element acts as a parasitic element that significantly enhances the isolation between the antennas and improves the overall impedance bandwidth of the system. In the back view of the SD-MIMO antenna, it is noteworthy that there is no gap between the partial ground planes of the two antennas. This design feature helps in maintaining consistent performance and minimizing interference between the antennas.

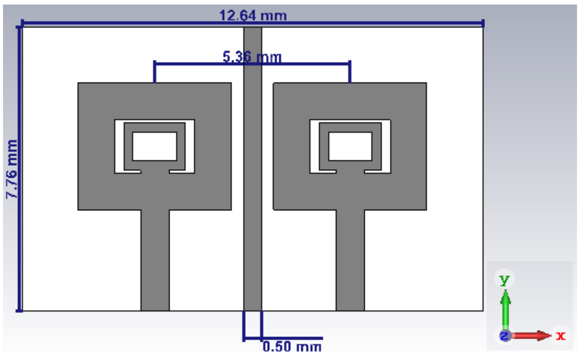

(a)

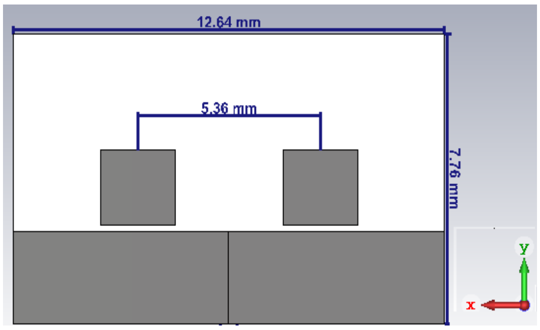

(b)

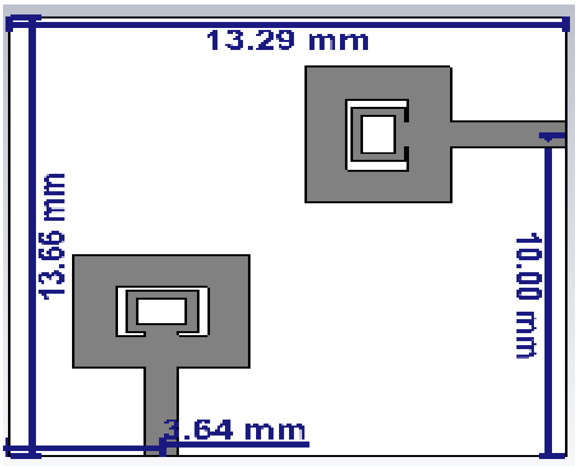

(c)

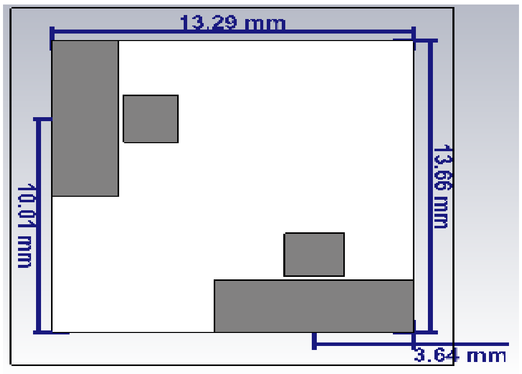

(d)

Fig. 9: (a) Front view of SD-MIMO (b) Back view of SD-MIMO (c) Front view of PD-MIMO (d) Back view of PD-MIMO Antenna

On the other hand, the PD-MIMO (Polarization Diversity Multiple Input Multiple Output) antenna features a different arrangement where the two antenna elements are oriented orthogonally to each other. This orthogonal placement allows the PD-MIMO antenna to exploit polarization diversity, which can enhance the system's overall performance by improving signal quality and reducing potential multipath interference.

Figure 10 shows a scattering parameter plot for both antennas. SD MIMO antennas have fewer than -10 dB reflection coefficients from 9.8 GHz to 40 GHz, 62.1 to 72.5 GHz, and 89 GHz to 95 GHz. Mutual coupling is less than -12 dB in all operational bands, and after 20 GHz it is less than -20 dB, indicating strong isolation. The PD MIMO antenna works from 13.5 GHz to 40 GHz, 62 GHz to 71 GHz, and 87.5 GHz to 95 GHz. Mutual coupling of the PD MIMO antenna is less than -15 dB, indicating strong diversity performance.

The MIMO performance parameters depicted in Fig. 11 provide a comprehensive evaluation of the antenna systems' effectiveness across various metrics. Figure 11(a) illustrates the Total Active Reflection Coefficient (TARC) for both MIMO antennas. The TARC values are consistently below 0 dB across the entire operating range, which signifies excellent impedance matching in the MIMO environment. This low TARC indicates that both antennas maintain efficient power transfer and minimal reflection, thereby optimizing their performance in practical scenarios.

Figure 11(b) presents the Channel Capacity Loss plot, where the loss values are less than 0.3 across the full operating band for both antennas. This low channel capacity loss reflects minimal signal degradation and suggests that the antennas achieve high efficiency in data transmission, preserving the integrity of the communication channel even under varying conditions.

The Envelope Correlation Coefficient is depicted in Fig. 11(c) and is approximately 0 for both antennas. This value indicates that the antennas are nearly independent of each other, which is crucial for minimizing interference and maximizing the diversity gain. Low envelope correlation implies that the antennas are well-suited for MIMO applications where independence between antenna elements is necessary for optimal performance.

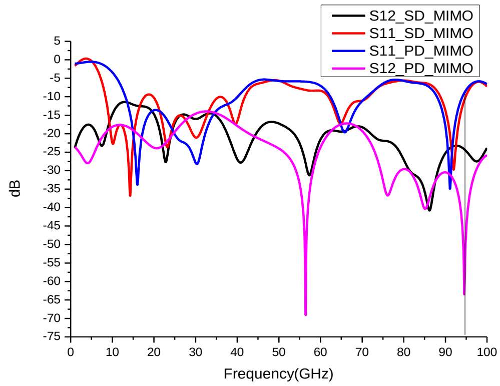

Fig. 10: Scattering parameter plot for SD MIMO and PD MIMO Antenna

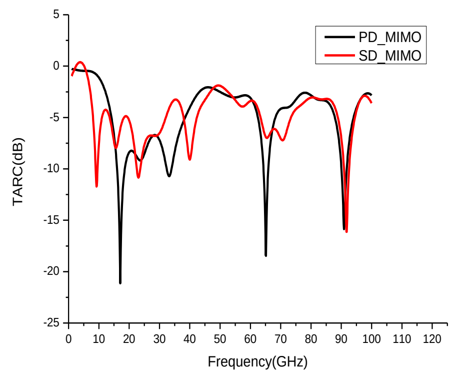

(a)

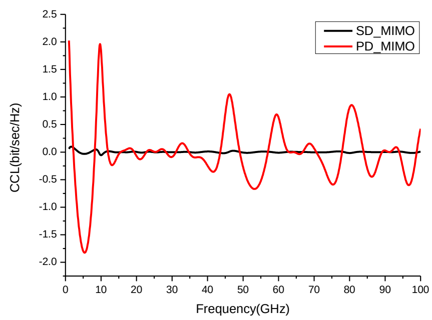

(b)

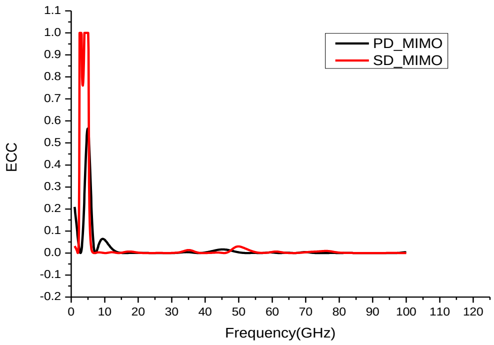

(c)

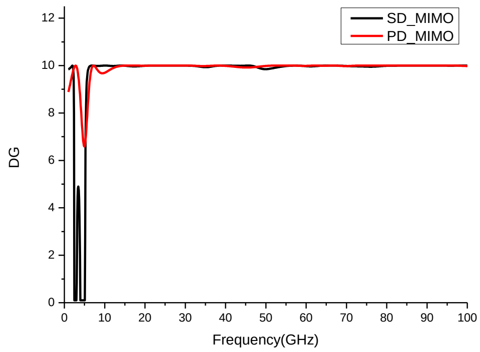

(d)

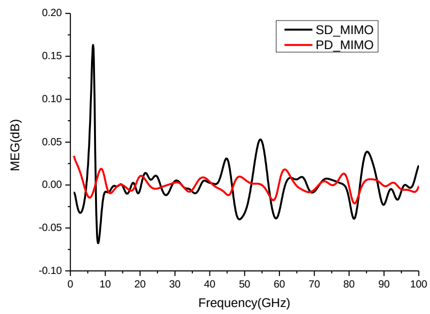

(e)

Fig. 11: MIMO parameters of SD-MIMO and PD-MIMO antenna (a) Total active reflection coefficient (TARC) (b) Channel capacity loss (CCL) (c) Envelope correlation coefficient (ECC) (d) Diversity gain (DG) (e) Mean effective gain (MEG)

In Figure 11(d), the Diversity Gain is shown to be approximately 10 across the entire frequency range for both antennas. This consistent diversity gain demonstrates that the antennas provide significant improvement in signal reliability and robustness against signal degradation. Diversity gain of around 10 reflects effective utilization of spatial diversity, which enhances the overall performance of the MIMO system.

Additionally, the Mean Effective Gain (MEG) is analyzed under multipath fading conditions. MEG is defined as the ratio of the received mean power of the diversity antenna to the received mean power of an isotropic antenna. The MEG values for both antennas are consistently less than 0.5 across the operating band, indicating that the antennas exhibit good diversity performance. Lower MEG values further confirm that the antennas are effective in mitigating the adverse effects of multipath fading, which is essential for maintaining reliable communication in challenging environments.

Overall, the performance parameters presented in Fig. 11 highlight that both MIMO antennas achieve excellent impedance matching, low channel capacity loss, high diversity gain, and effective performance under multipath conditions. These characteristics collectively demonstrate the antennas' strong performance and suitability for advanced MIMO applications.

8. Applications of proposed antenna in healthcare

IoMT devices (implantable medical devices, remote sensing and monitoring in home and various wearables), handling of big data generated by health sensors, smart wearable devices to remotely monitor various health parameters such as heart beat rate, basic blood pressure, breathing rate, blood sugar, internal organ temperature, etc.), tumor detection, military communication, spectroscopy, remote sensing, enviroscopy, and environmental monitoring are some of the applications that the proposed antenna is able to support[52)]

Covid'19 has been proclaimed a worldwide public health emergency. Numerous patients were unable to get medical care owing to the large number of sick persons, and numerous clinicians contracted the virus while treating patients as a result of the infected patients' widespread viral transmission[53)]. Discovering remote detection techniques for COVID'19 requires the use of lightweight, affordable handheld devices[3,54)]. Researchers have suggested utilizing a metamaterial-based mm-wave resonator to detect infectious disease. By assessing the dielectric qualities of blood samples, the disposable top layer may detect dengue. When a patient had dengue, as opposed to a healthy patient, the sensor noted a drop in blood permittivity[55)]. According to[56)], COVID-19 disease occurs ground-glass opacification in the lungs. These opacification suggest a discrepancy in the dielectric characteristics of the affected tissues compared to the surrounding healthy tissues[57)]. Thus, given that these opacification are greater than lung tumors, microwave imaging might find them[58)]. This study describes the use of a suggested antenna to monitor fluctuations in blood dielectric constant and detections of differences in lung dielectric properties owing to lung infections, which led to the detection of COVID'19 infections.

This section outlines the use of an antenna to monitor variations in blood dielectric constant and lung dielectric characteristics due to lung infections, which may also led to the detection of COVID'19 infections.

Testing vitals including blood sugar, blood pressure, and oxygen levels is common procedure in hospitals since it gives doctors valuable information about a patient's health. Regular blood glucose testing using an invasive instrument is crucial for treating diabetes, but it's uncomfortable, unpleasant, and doesn't allow for continuous monitoring. Hyper- and hypoglycemia may occur between finger-prick examinations. Noninvasive glucose measurement devices are needed. Ultrasound-based measurement, reverse iontophoresis, infrared spectroscopy, bioimpedance spectroscopy, ocular spectroscopy, etc. are only a few of the solutions that have been proposed; nevertheless, these technologies have a number of drawbacks in terms of stability, safety, and mobility[59)]. A new generation of electromagnetism-based sensors are making continuous monitoring of blood glucose levels possible without requiring intrusive procedures and putting patients in a heightened state of anxiety or discomfort. The quantity of substances like blood glucose in a blood sample affects the sample's complex permittivity. Blood containing sugar has a lower dielectric constant than normal blood. Dielectric constant represents The glucose levels are determined by using and analyzing the qualities of the reflected and transmitted waves in terms of scattering parameters or S parameters[59,60)]. Scattering parameter variation may be related to variations in substance concentration and is a function of the dielectric constant along the signal path[60)]. Changes in glucose levels may be measured by calibrating the connection between variation in reflection coefficient and variation in dielectric constant of blood for normal patients and diabetic patients. According to[61)]'s tests, the antenna's performance characteristics are dependent not only on its physical specifications but also on the dielectric constant of the high loss medium, which is the human body when the antenna is placed near the human hand. Normal patients have blood glucose levels of about 100 mg/dl, while diabetic patients have blood glucose levels of more than 126 mg/dl. The hypo- to hyperglycemic range is indicated by glucose concentration changes of 10 mg/dl[61)].

Table 7. Electrical properties of biological layers

Tissue	Dielectric constant	Electric conductivity(S/m)
Fat Layer	5.46	0.051
Skin Layer	43.75	0.856
Blood Layer	79	1.538

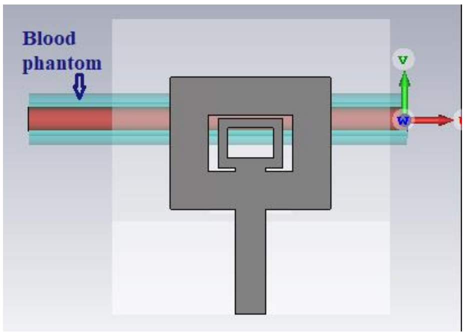

Fig. 12: Application of proposed antenna in Blood Sugar fluctuation measurement

In order to show what the proposed antenna could do for non-invasive wireless blood sugar monitoring(as shown in Fig. 12), a concentric biological phantom[62)] was made in the CST Microwave studio. It has a blood layer 2.5 mm in diameter, an outer fat layer 0.5 mm thick, and an outer skin layer 1 mm thick. The earlobe phantom used in[63)] was utilized to determine the appropriate thickness of the different tissue layers employed in the biological model.[63)] modelled a five-layer boxing earlobe phantom, whereas our study used a three-layer concentric phantom, as shown in Fig. 13. Phantom only displays a blood vasculature covered by a skin layer and a layer of intermediate fat. The measuring site may be the hand, earlobe, or another location, but the antennas must detect the change in dielectric constant of the blood layer after penetrating the outer skin layer and the fat layer. The Cole-Cole dispersive dielectric models of various tissues may be used to depict the structure of this homogeneous multilayer phantom, as detailed in[64)]. Electrical properties of biological layers are presented in Table 7.

The observations of S 11 and resonant frequency for blood dielectric constants 76,77,78, and 79 are presented in Table 8. In the Table 8, Fr1, Fr2, Fr3, Fr4, Fr5: first, second, third, fourth, fifth resonant frequency respectively and unit is Hz. S 11_1, S 11_2, S 11_3, S 11_4 and S 11_5 are reflection coefficients in dB at Fr1, Fr2, Fr3, Fr4, Fr5. It can be observed that significant fluctuations occur in both the S 11 parameter and the resonant frequencies when the dielectric constant of blood decreases from the normal value of 79. Specifically, a reduction in the dielectric constant results in a noticeable shift of the resonance frequencies to higher values. This upward shift in resonance frequencies corresponds to a decrease in the dielectric constant, which affects how the antenna interacts with the blood sample. When analyzing the S 11 parameter, which represents the reflection coefficient of the antenna, there are clear changes observed at different resonant frequencies. At $Fr1$ and $Fr3$, S 11 increases as the dielectric constant decreases, indicating a higher level of signal reflection at these frequencies. This suggests that the antenna's impedance matching is deteriorating with lower dielectric constants at these points. At $Fr2$, an increase in S 11 is noted for all dielectric constants tested, except for the dielectric constant of 79. This implies that the reflection characteristics at this frequency are sensitive to variations in the dielectric constant, with a distinct change in behavior observed only for the normal dielectric value. Additionally, fluctuations in S 11 and resonant frequency at $Fr4$ do not follow the expected patterns.

These deviations suggest that the response at this frequency is less predictable and may be influenced by other factors beyond just the dielectric constant. Interestingly, at the fifth resonant frequency ($Fr5$), S 11 shows a notable increase when the dielectric constant is 76 compared to other values. This implies that the antenna's response at this frequency is particularly sensitive to changes in the dielectric constant around this value. By integrating the response data obtained across several resonant frequencies, it is possible to detect and analyze variations in the dielectric constant of blood or blood sugar levels more effectively. The combined information from multiple frequency bands provides a comprehensive picture of how the dielectric properties of the blood change, which can be useful for accurate monitoring and diagnostics

It can be observed that significant fluctuations occur in both the S 11 parameter and the resonant frequencies as the dielectric constant of blood decreases from the normal value of 79. This value is considered to represent normal blood or a glucose concentration of 0 mole. When the dielectric constant drops to

78, which corresponds to a change in glucose concentration of 0.005 mole, noticeable effects on the antenna's performance are observed.

The purpose of this section is to evaluate the proposed antenna's potential to perceive lung COVID-19 infection through reflection coefficient measurements using specialized phantoms (As shown in Fig.14) that related to dielectric characteristics of a human torso and contain a target that simulates an infection. Frequency-domain measurements have been carried out in CST Microwave Studio to acquire the reflection coefficient in order to identify the Lung COVID-19 infection within a human torso phantom (S 11).This section's goal is to assess the proposed antenna's ability. Human torso phantom has first been created in CST Microwave Studio by taking into account dielectric constant and conductivity. The works seen in[58,65], which was composed of two layers with an elliptical form, served as inspiration for the torso-mimicking phantom.

The works seen in[58,65], which were composed of two layers with an elliptical form, served as inspiration for the torso-mimicking phantom. The exterior layer's elliptical form represents the mixture of muscle, fat, and rib bone cells; it could be indicative of a small-size prototype chest circumference. The outer layer resembles a mixture of ribbone, muscle, and fat tissues. The interior layer is elliptic-shaped and resembles a lung cell.

Table 8. S 11 and resonant frequency observations for various types of blood

Dielectric constant of blood	Mole fraction of Glucose	Fr1	S 11_1	Fr2	S 11_2	Fr3	S 11_3	Fr4	S 11_4	Fr5	S 11_5
76	0.015	15.354	-35.6213	24.265	-47.113	34.066	-26.359	65.35	-22.708	91.585	-39.886
77	0.010	15.355	-35.6955	24.265	-45.774	34.066	-27.122	65.35	-22.662	91.585	-43.358
78	0.005	15.355	-35.9375	24.166	-47.833	33.967	-27.825	65.35	-22.662	91.486	-43.11
79	0	15.355	-36.13005	24.166	-45.532	33.868	-28.587	65.251	-22.578	91.486	-43.0184

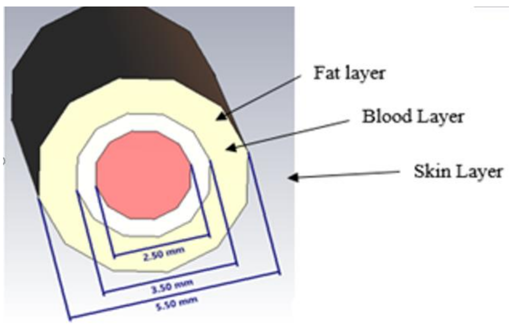

Fig. 13: Proposed antenna with simulated phantom

The major and minor diameters of the outer elliptical layer are 60 mm and 30 mm, respectively, with a dielectric constant of 53.3, which represents a mixture of muscle, fat, and rib bone cells. Major and minor diameters of the mid-elliptical layer are 40 mm and 10 mm, respectively, with a dielectric constant of 20, which represents the lung. The innermost cylinder has a diameter of 2 mm and a dielectric constant of 78, which represents lung infection. As shown in Fig. 14, a tiny cylindrical substance has been put on the inner layer's wall to mimic a lung infection. The real dimension may vary from the measured dimension of the Torso-mimicking phantom used as an example. Identical to[65], tap water was employed as a substance to imitate lung diseases. The conductivity and dielectric constant of actual tissues are shown in Table 9, which is obtained from[65–67]. Table 10 displays the observation of reflection coefficients for both diseased and normal lungs at various resonance frequencies. The resonance frequencies and reflection coefficients of the infected and normal lungs (lungs with stored water) differ noticeably. When lung infection occurs in the first and third resonating bands, the resonant frequency shifts towards a higher range. The resonant frequencies remain unchanged in the second and fifth bands.

The resonance frequency only slightly increases in the fourth band.

Table 9. Dielectric properties of actual tissues[65–67]

Tissues	Conductivity(S/m)	Dielectric Constant
Fat	0.03	5.33
Muscle tissue	1.45	53.3
Lung inflated	0.1	20
Rib bone tissue	0.3	11.7
Lung lesion	1.59	78

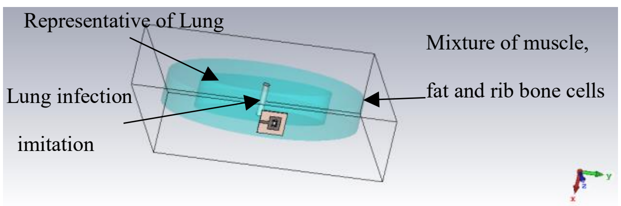

Fig. 14: Application of proposed antenna in lung infection detection measurement

Infected lung decreases S 11 at the second, fourth, and fifth bands; variations are out of band at the first and third trends. When responses are compared across other bands, most results demonstrate notable differences in resonant frequency and S 11, which unmistakably point to a lung infection. The results of the study suggest that the proposed antenna can be used to detect the COVID-19 virus and interact wirelessly with patients. This is supported by the measurements of S 11 variations between healthy and infected lungs, as well as the decrease in blood dielectric constant caused by elevated blood sugar levels.

Table 10. S 11 and resonant frequency observations for Normal lung and infected lung

Lung	**Fr1**	**S 11_1**	**Fr2**	**S 11_2**	**Fr3**	**S 11_3**	**Fr4**	**S 11_4**	**Fr5**	**S 11_5**
Normal Lung	16.376	-11.206	22.582	-39.14	28.506	-24.399	65.44	-20.071	89.11	-17.495
Infected Lung	16.38	-10.507	22.582	-39.58	28.621	-23.06	65.152	-21.519	89.11	--18.358

9. Conclusion

This paper proposes a multi-band shared aperture planar antenna; its 16-element phased array, spatial diversity, and pattern diversity configurations are presented. The proposed antenna array provides ultra-wide band characteristics from 12.991 to 39.966 GHz with a gain of 15.2 dB and 16.9 dB at 28 GHz and 38 GHz, a second resonance from 62.114 to 70.452 GHz with a gain of 14.3 dB at 66 GHz, a third resonance from 88.04 to 94.7 GHz with a gain of 13.4 dB at 92 GHz, and a fourth resonance from 0.24-1 THz with a gain of 25.5 dB at 0.546 THz. Broad bandwidth, high gain, narrow beam radiation pattern, low side lobe levels, and wide beam steering range meet the needs of 5G and beyond wireless communication, as well as numerous healthcare services. The antenna's gain varies by less than 5 dB across its working range. The single-layer steerable narrow beam antenna has a thickness of just 0.254 mm and an area of 8.518×72.77 mm^2, meeting the requirements for low profile, planer, cost efficiency, and compact size. The low profile, small dimensions, and planar geometry decrease production costs. Spatial diversity and polarization diversity A MIMO antenna has been presented for 5G success points or base stations, which provides good isolation and impedance bandwidth and acceptable diversity parameters. The presented antenna covers the majority of the 5G mm-wave band, Wi-Gig band, Ku band of satellite communication, W-band, and sub-THz spectrum. The suggested antenna's performance is compared to that of previously reported mm-wave antennas at 28 GHz, 38 GHz, 66 GHz, and 92 GHz. It provides superior performance in operating bands. It could be a good candidate for future fifth-generation and beyond cellular communications, Wi-Gig, Ku band satellite communication, device-to-device communication (D2D communication), mission-critical push-to-talk communication (MCPTT), vehicle-to-anything communication (V2X), and many other applications. The proposed antenna array could be used for a variety of health care applications, including remote monitoring of COVID patients, remote health care services, wireless monitoring of blood sugar detection, driverless ambulances, efficient indoor communication in a crowded hospital environment, mm-wave and tera-wave imaging and spectroscopy, AR-VR-based healthcare services, remote drug delivery, automatic facture detection, remote robotic surgery, and many others, to help control a pandemic situation like COVID'19. The suggested antenna has been employed to demonstrate the detection of lung infections and COVID-19 utilizing measurements of blood sugar variations. When comparing the normal and infected sugar levels or water content in the lung phantom, the proposed antenna successfully displays the differences in resonant frequency and S 11.

References

1) Osaka University, "Terahertz accelerates beyond 5g towards 6g," *ScienceDaily*, (2021). %3Cwww.sciencedaily.com/releases/2021/02/210203162302.htm%3E. (accessed February 3, 2021).
2) Michael Tice, "Terahertz spectroscopy opens options in covid-19 screening," *LabPulse.Com*, (2020). Terahertz spectroscopy opens options in COVID-19 screening.
3) T. Nahar, and S. Rawat, "Millimeter-wave planar antennas for 5g-based remote monitoring and treatment of covid-19 patients," *Trans. Emerg. Telecommun. Technol.*, **n/a** (*n/a*) e4426 (n.d.). doi:https://doi.org/10.1002/ett.4426.
4) C. Apriono, H.T. Andhyka, and F.Y. Zulkifli, "Effects of polarization and different tissue on terahertz cancer imaging," *Evergreen*, **11**(*1*) 525–535 (2024). doi:10.5109/7172318
5) D. Haider, A. Ren, D. Fan, N. Zhao, X. Yang, S.A.K. Tanoli, Z. Zhang, F. Hu, S.A. Shah, and Q.H. Abbasi, "Utilizing a 5g spectrum for health care to detect the tremors and breathing activity for multiple sclerosis," *Trans. Emerg. Telecommun. Technol.*, **29** (*10*) e3454 (2018). doi:https://doi.org/10.1002/ett.3454.
6) Y. Siriwardhana, G. Gür, M. Ylianttila, and M. Liyanage, "The role of 5g for digital healthcare against covid-19 pandemic: opportunities and challenges," *ICT Express*, **7** (*2*) 244–252 (2021). doi:10.1016/j.icte.2020.10.002.
7) R. Singh, W. Lehr, D. Sicker, and K.M.S. Huq, "Beyond 5g: the role of thz spectrum," *SSRN Electron. J.*, (*January*) (2019). doi:10.2139/ssrn.3426810.
8) I. Utama, Y.R. Hasian Aruan, Rochmawati, R.F. Sari, and R. Harwahyu, "5G mmwave network performance evaluation with blockage simulation," *Evergreen*, **9**(*4*) 1236–1243 (2022). doi:10.5109/6625735.

9) V. Prakash, L. Garg, L. Camilleri, J. Curmi, and D. Camilleri, "5G in healthcare," 51–68 (2021). doi:10.4018/978-1-7998-6988-7.ch004.
10) R.K. Kushwaha, and P. Karuppanan, "Design and analysis of vivaldi antenna with enhanced radiation characteristics for mm-wave and thz applications," *Opt. Quantum Electron.*, **51** (*9*) 309 (2019). doi:10.1007/s11082-019-2032-4.
11) A. Gupta, A. Kansal, and P. Chawla, "A survey and classification on applications of antenna in health care domain: data transmission, diagnosis and treatment," *Sādhanā*, **46** (*2*) 68 (2021). doi:10.1007/s12046-021-01586-4.
12) R. Elsharkawy, M. Hindy, A.-R. Sebak, A. Saleeb, E.-S.M. El-Rabaie, A.M.R. Ragheb, M. Ashraf, and S. Alshebeili, "Single- and double-beam reflectarrays for ka band communication," *Sādhanā*, **44** (*5*) 106 (2019). doi:10.1007/s12046-019-1109-x.
13) T. Nahar, and S. Rawat, "Survey of various bandwidth enhancement techniques used for 5g antennas," *Int. J. Microw. Wirel. Technol.*, 1–21 (2021). doi:10.1017/S1759078720001804.
14) T. Nahar, and S. Rawat, "Low Cost Planar Millimeter Wave Antenna Array for 5G Mobile Applications," in: 2020 2nd Int. Conf. Adv. Comput. Commun. Control Netw., 2020: pp. 621–626. doi:10.1109/ICACCCN51052.2020.9362828.
15) C. Zhao, Y. Bai, and Q. Wei, "A 2 to 50 ghz all-metal vivaldi antenna for ultra-wideband (uwb) application," *AEU - Int. J. Electron. Commun.*, **148** 154162 (2022). doi:https://doi.org/10.1016/j.aeue.2022.154162.
16) N. Shukla, and A. Saigal, "Modal analysis of ananomechanical antenna structure in mhz—ghzrange," *Int. J. Model. Simul.*, **30** (*1*) 22–29 (2010). doi:10.1080/02286203.2010.11442554.
17) A. Djellid, F. Benmeddour, L. Bahri, and A. Ghodbane, "Novel high-gain and compact uwb microstrip antenna for wifi, wimax, wlan, x band and 5g applications," *Opt. Quantum Electron.*, **54** (*7*) 441 (2022). doi:10.1007/s11082-022-03731-7.
18) A.A. Ibrahim, and W.A.E. Ali, "High gain, wideband and low mutual coupling amc-based millimeter wave mimo antenna for 5g nr networks," *AEU - Int. J. Electron. Commun.*, **142** 153990 (2021). doi:https://doi.org/10.1016/j.aeue.2021.153990.
19) M. Abri, N. Boukli-Hacene, and F.T. Bendimerad, "Synthesis of ring printed antennas arrays: optimization by the genetic algorithm," *Int. J. Model. Simul.*, **28** (*2*) 174–181 (2008). doi:10.1080/02286203.2008.11442465.
20) S. Vasana, "Modelling and simulation of the conversion of correlated and unbalanced antenna diversity systems," *Int. J. Model. Simul.*, **28** (*1*) 80–84 (2008). doi:10.1080/02286203.2008.11442453.
21) S. Farhat, F. Arshad, Y. Amin, and J. Loo, "Wideband patch array antenna using superstrate configuration for future 5g applications," *Turkish J. Electr. Eng. Comput. Sci.*, **28** (*3*) 1673–1685 (2020). doi:10.3906/elk-1910-160.
22) M.M.M. Ali, and A.-R. Sebak, "Design of compact millimeter wave massive MIMO dual-band (28/38 GHz) antenna array for future 5G communication systems," in: 2016 17th Int. Symp. Antenna Technol. Appl. Electromagn., 2016: pp. 1–2. doi:10.1109/ANTEM.2016.7550213.
23) K. Mahmoud, and A. Montaser, "Optimised 4x4 millimetre wave antenna array with dgs using hybrid ecfo-nm algorithm for 5g mobile networks," *IET Microwaves, Antennas Propag.*, **11** (2017). doi:10.1049/iet-map.2016.0959.
24) E. Garcia-Marin, J.L. Masa-Campos, and P. Sanchez-Olivares, "Diffusion bonding manufacturing of high gain w-band antennas for 5g applications," *IEEE Commun. Mag.*, **56** (*7*) 21–27 (2018). doi:10.1109/MCOM.2018.1700986.
25) S.F. Jilani, and A. Alomainy, "A multiband millimeter-wave 2-d array based on enhanced franklin antenna for 5g wireless systems," *IEEE Antennas Wirel. Propag. Lett.*, **16** 2983–2986 (2017). doi:10.1109/LAWP.2017.2756560.
26) H. Shawkey, and D. Elsheakh, "Multiband dual-meander line antenna for body-centric networks' biomedical applications by using umc 180 nm," *Electron.*, **9** (*9*) 1–11 (2020). doi:10.3390/electronics9091350.
27) Y. Albagory, "An efficient wban aggregator switched-beam technique for isolated and quarantined patients," *AEU - Int. J. Electron. Commun.*, **123** 153322 (2020). doi:https://doi.org/10.1016/j.aeue.2020.153322.
28) N.R. Philip, and M. Balakrishnan, "Beam-aware energy harvesting discontinuous reception in machine-to-machine millimeter-wave 5g communications," *Int. J. Commun. Syst.*, **33** (*16*) e4567 (2020). doi:https://doi.org/10.1002/dac.4567.
29) M.K. Sharma, and A. Sharma, "Compact size easily extendable self isolated multi-port multi-band antenna for future 5g high band and sub-thz band applications," *Opt. Quantum Electron.*, **55** (*2*) 146 (2022). doi:10.1007/s11082-022-04313-3.
30) M.H. Mickle, M. Mi, C.C. Capelli, H. Swift, J.T. Cain, and D.W. Sammel, "Energy harvesting antennas or when is a monopole half of a dipole?," *Int. J. Model. Simul.*, **27** (*3*) 266–272 (2007). doi:10.1080/02286203.2007.11442426.
31) R. Xu, S. Gao, B.S. Izquierdo, C. Gu, P. Reynaert, A. Standaert, G.J. Gibbons, W. Bösch, M.E. Gadringer, and D. Li, "A review of broadband low-cost and high-gain low-terahertz antennas for wireless communications applications," *IEEE Access*, **8** 57615–57629 (2020). doi:10.1109/ACCESS.2020.2981393.
32) A. Bindle, T. Gulati, and N. Kumar, "A detailed introduction of different beamforming techniques used in 5g," *Int. J. Commun. Syst.*, **34** (*5*) e4718 (2021). doi:https://doi.org/10.1002/dac.4718.
33) J. Lota, S. Sun, T.S. Rappaport, and A. Demosthenous,

"5G uniform linear arrays with beamforming and spatial multiplexing at 28, 37, 64, and 71 ghz for outdoor urban communication: a two-level approach," *IEEE Trans. Veh. Technol.*, **66** (*11*) 9972–9985 (2017). doi:10.1109/TVT.2017.2741260.

34) "CST microwave studio," (n.d.). http://www.cst.com/products/cstmws.

35) X. Ruan, and C.H. Chan, "Terahertz free-space dielectric property measurements using time- and frequency-domain setups," *Int. J. RF Microw. Comput. Eng.*, **29** (*9*) 1–9 (2019). doi:10.1002/mmce.21839.

36) B. Yu, K. Yang, C. Sim, and G. Yang, "Communication with metallic casing application," *IEEE Trans. Antennas Propag.*, **66** (*1*) 462–466 (2018).

37) M. Mantash, and T.A. Denidni, "CP antenna array with switching-beam capability using electromagnetic periodic structures for 5g applications," *IEEE Access*, **7** 26192–26199 (2019). doi:10.1109/ACCESS.2019.2901440.

38) I. Aziz, R. Dahlbäck, E. Öjefors, A. Rydberg, and D. Dancila, "High gain compact 57–66 GHz antenna array for backhaul amp; access communications," in: 12th Eur. Conf. Antennas Propag. (EuCAP 2018), 2018: pp. 1–4. doi:10.1049/cp.2018.0362.

39) I. Aziz, R. Dahlback, E. Ojefors, K. Sjogren, A. Rydberg, and D. Dancila, "60 ghz compact broadband antenna arrays with wide-angle beam steering," *J. Eng.*, **2019** (2019). doi:10.1049/joe.2018.5343.

40) T. Zhang, L. Li, M. Xie, H. Xia, X. Ma, and T.J. Cui, "Low-cost aperture-coupled 60-ghz-phased array antenna package with compact matching network," *IEEE Trans. Antennas Propag.*, **65** (*12*) 6355–6362 (2017). doi:10.1109/TAP.2017.2722867.

41) D. Zelenchuk, A.J. Martinez-Ros, T. Zvolensky, J.L. Gomez-Tornero, G. Goussetis, N. Buchanan, D. Linton, and V. Fusco, "W-band planar wide-angle scanning antenna architecture," *J. Infrared, Millimeter, Terahertz Waves*, **34** (*2*) 127–139 (2013). doi:10.1007/s10762-013-9960-z.

42) H. Vettikalladi, M.K. Saleem, and M.A.S. Alkanhal, "Membrane antenna array based on substrate integrated waveguide technology for 94 ghz communication systems," *Int. J. Microw. Wirel. Technol.*, **8** (*3*) 633–641 (2016). doi:10.1017/S1759078715000240.

43) W.-Y. Uhm, K.-K. Ryu, and S.-C. Kim, "A 94-ghz phased array antenna using a log-periodic antenna on a gaas substrate," *J. Inf. Commun. Converg. Eng.*, **13** (*2*) 81–85 (2015). doi:10.6109/jicce.2015.13.2.081.

44) B. Aqlan, M. Himdi, H. Vettikalladi, and L. Le-Coq, "A 300-ghz low-cost high-gain fully metallic fabry–perot cavity antenna for 6g terahertz wireless communications," *Sci. Rep.*, **11** (*1*) 7703 (2021). doi:10.1038/s41598-021-87076-3.

45) T. Tajima, H.-J. Song, K. Ajito, M. Yaita, and N. Kukutsu, "300-ghz step-profiled corrugated horn antennas integrated in ltcc," *IEEE Trans. Antennas Propag.*, **62** (*11*) 5437–5444 (2014). doi:10.1109/TAP.2014.2350520.

46) H. Vettikalladi, W.T. Sethi, A.F. Bin Abas, W. Ko, M.A. Alkanhal, and M. Himdi, "Sub-thz antenna for high-speed wireless communication systems," *Int. J. Antennas Propag.*, **2019** 9573647 (2019). doi:10.1155/2019/9573647.

47) C.X. Mao, M. Khalily, P. Xiao, T.W.C. Brown, and S. Gao, "Planar sub-millimeter-wave array antenna with enhanced gain and reduced sidelobes for 5g broadcast applications," *IEEE Trans. Antennas Propag.*, **67** (*1*) 160–168 (2019). doi:10.1109/TAP.2018.2874796.

48) S. Zhu, H. Liu, and P. Wen, "A new method for achieving miniaturization and gain enhancement of vivaldi antenna array based on anisotropic metasurface," *IEEE Trans. Antennas Propag.*, **67** (*3*) 1952–1956 (2019). doi:10.1109/TAP.2019.2891220.

49) M. Khalily, R. Tafazolli, T. A. Rahman and M. R. Kamarudin, "Design of Phased Arrays of Series-Fed Patch Antennas With Reduced Number of the Controllers for 28-GHz mm-Wave Applications," in IEEE Antennas and Wireless Propagation Letters, 15 1305-1308 (2016). doi: 10.1109/LAWP.2015.2505781.

50) A.C. Sodré, I.F. da Costa, R.A. dos Santos, H.R.D. Filgueiras, and D.H. Spadoti, "Waveguide-based antenna arrays for 5g networks," *Int. J. Antennas Propag.*, **2018** 5472045 (2018). doi:10.1155/2018/5472045.

51) B. Aghoutane, S. Das, M. EL Ghzaoui, B.T.P. Madhav, and H. El Faylali, "A novel dual band high gain 4-port millimeter wave mimo antenna array for 28/37 ghz 5g applications," *AEU - Int. J. Electron. Commun.*, **145** 154071 (2022). doi:https://doi.org/10.1016/j.aeue.2021.154071.

52) "The fcc ' s 5g fast plan," (*1*) 5 (2019).

53) V.K. Yadav, V.K. Yadav, and J.P. Yadav, "Cognizance on pandemic corona virus infectious disease (covid-19) by using statistical technique: a study and analysis," *Evergreen*, **7**(*3*) 329–335 (2020). doi:10.5109/4068611

54) A. Akinola, G. Singh, and A. Ndjiongue, "Frequency-domain reconfigurable antenna for covid-19 tracking," *Sensors Int.*, **2** (*March*) 100094 (2021). doi:10.1016/j.sintl.2021.100094.

55) S. Asghar Qureshi, Z. Zainal Abidin, H. A. Majid, A.Y.I. Ashyap, and C. Hwang See, "Double-layered metamaterial resonator operating at millimetre wave for detection of dengue virus," *AEU - Int. J. Electron. Commun.*, **146** 154134 (2022). doi:https://doi.org/10.1016/j.aeue.2022.154134.

56) H. Shi, X. Han, N. Jiang, Y. Cao, O. Alwalid, J. Gu, Y. Fan, and C. Zheng, "Radiological findings from 81 patients with covid-19 pneumonia in wuhan, china: a descriptive study," *Lancet Infect. Dis.*, **20** (*4*) 425–

434 (2020). doi:10.1016/S1473-3099(20)30086-4.

57) X. Lin, Z. Gong, Y. Ding, Y. Chen, P.A. Valdes Sosa, and M. Joseph Valdes Sosa, "Feasibility Study of Detection of Coronavirus Disease 2019 with Microwave Medical Imaging," in: 2021 15th Eur. Conf. Antennas Propag., 2021: pp. 1–4. doi:10.23919/EuCAP51087.2021.9411374.
58) B. Khalesi, B. Khalid, N. Ghavami, S. Dudley, M. Ghavami, and G. Tiberi, "Microwave imaging for lung covid-19 infection detection through huygens principle," *Prog. Electromagn. Res. Symp.*, **2021-Novem** 2885–2891 (2021). doi:10.1109/PIERS53385.2021.9694816.
59) J. Kost, S. Mitragotri, R.A. Gabbay, M. Pishko, and R. Langer, "Transdermal monitoring of glucose and other analytes using ultrasound," *Nat. Med.*, **6** (*3*) 347–350 (2000). doi:10.1038/73213.
60) S. Saha, H. Cano-Garcia, I. Sotiriou, O. Lipscombe, I. Gouzouasis, M. Koutsoupidou, G. Palikaras, R. Mackenzie, T. Reeve, P. Kosmas, and E. Kallos, "A glucose sensing system based on transmission measurements at millimetre waves using micro strip patch antennas," *Sci. Rep.*, **7** (*1*) 1–11 (2017). doi:10.1038/s41598-017-06926-1.
61) J. Hanna, M. Bteich, Y. Tawk, A.H. Ramadan, B. Dia, F.A. Asadallah, A. Eid, R. Kanj, J. Costantine, and A.A. Eid, "Noninvasive, wearable, and tunable electromagnetic multisensing system for continuous glucose monitoring, mimicking vasculature anatomy," *Sci. Adv.*, **6** (*24*) 1–11 (2020). doi:10.1126/sciadv.aba5320.
62) CST, "CST studio suite - electromagnetic field simulation software," *CST Comput. Simul. Technol. AG*, (2016).
63) F. Wang, "Microwave-based non-invasive blood glucose levels monitoring using flexible uwb antennas," *IET Conf. Publ.*, **2018** (*CP741*) 5–8 (2018). doi:10.1049/cp.2018.1223.
64) A. Elkady, M. El-Hadidy, A. Medhat, A. Khorshid, and A. Darwish, "Microwave power absorption in human body for non-invasive glucose monitoring," *Prog. Electromagn. Res. Symp.*, (*February 2015*) 109–113 (2013).
65) B. Khalesi, B. Khalid, N. Ghavami, G. Raspa, M. Ghavami, S. Dudley-Mcevoy, and G. Tiberi, "A microwave imaging procedure for lung lesion detection: preliminary results on multilayer phantoms," *Electron.*, **11** (*13*) 1–10 (2022). doi:10.3390/electronics11132105.
66) P. Hasgall, E. Neufeld, M.-C. Gosselin, A. Klingenböck, and N. Kuster, "ITIS database for thermal and electromagnetic parameters of biological tissues, version 2.2," *Sept. 26th*, (2011).
67) S Gabriel, R W Lau, and C Gabriel, "The dielectric properties of biological tissues: iii. parametric models for the dielectric spectrum of tissues," *Phys. Med. Biol.*, **41** (*11*) 2271 (1996). doi:10.1088/0031-9155/41/11/003.